The Astrophysical Journal, 908:138 (10pp), 2021 February 20 https://doi.org/10.3847/1538-4357/abdab2


# Role of Polycyclic Aromatic Hydrocarbons on the Cosmic-Ray Ionization Rate in the Galaxy

Gargi Shaw[1] and G. J. Ferland[2]
[1] Department of Astronomy and Astrophysics, Tata Institute of Fundamental Research Homi Bhabha Road, Navy Nagar, Colaba, Mumbai 400005, India
gargishaw@gmail.com, gary@g.uky.edu
[2] Department of Physics and Astronomy, University of Kentucky Lexington, KY 40506, USA
*Received 2020 November 14; revised 2020 December 26; accepted 2021 January 10; published 2021 February 19*

## Abstract

The cosmic-ray (CR) ionization rate ($\zeta$, $s^{-1}$) plays an important role in the interstellar medium. It controls ion–molecular chemistry and provides a source of heating. Here we perform a grid of calculations using the spectral synthesis code CLOUDY along nine sightlines toward, HD 169454, HD 110432, HD 204827, $\lambda$ Cep, X Per, HD 73882, HD 154368, Cyg OB2 5, and Cyg OB2 12. The value of $\zeta$ is determined by matching the observed column densities of $H_3^+$ and $H_2$. The presence of polycyclic aromatic hydrocarbons (PAHs) affects the free electron density, which changes the $H_3^+$ density and the derived ionization rate. PAHs are ubiquitous in the Galaxy, but there are also regions where PAHs do not exist. Hence, we consider clouds within a range of PAH abundances and show their effects on the $H_3^+$ abundance. We predict an average CR ionization rate for $H_2$ ($\zeta(H_2)$) $= (7.88 \pm 2.89) \times 10^{-16}$ $s^{-1}$ for models with average Galactic PAH abundances, (PAH/H $= 10^{-6.52}$), except Cyg OB2 5 and Cyg OB2 12. The value of $\zeta$ is nearly 1 dex smaller for sightlines toward Cyg OB2 12. We estimate the average value of $\zeta(H_2) = (95.69 \pm 46.56) \times 10^{-16}$ $s^{-1}$ for models without PAHs.

*Unified Astronomy Thesaurus concepts:* Astrochemistry (75); Interstellar molecules (849); Interstellar medium (847); Photodissociation regions (1223)

## 1. Introduction

Cosmic-rays (CRs) are high-energy particles mostly made of protons whose energy ranges from a few megaelectronvolts to a few gigaelectronvolts. They penetrate deep into interstellar clouds and produce a primary ionization and a cascade of secondary ionizations (Spitzer & Tomasko 1968). The free electrons they produce heat the gas, and deep in the cloud they control the ion–molecular chemistry network in the absence of other ionizing sources. Hence, it is very important to determine the CR ionization rate ($\zeta$) for such environments. Several groups have estimated the value of $\zeta$ based on the abundances of various molecules such as HD (O'Donnell & Watson 1974) and $H_3^+$ (Indriolo & McCall 2012; Neufeld & Wolfire 2017). Interestingly, the value differs depending on the molecule involved. In the diffuse clouds, $\zeta$ is determined from the observed column densities of $H_3^+$, since it undergoes simple chemical reactions (McCall et al. 2003). However, $H_3^+$ undergoes a complex chain of chemical reactions in dense clouds (Dalgarno 2006), and the value of $\zeta$ is lower than that of diffuse clouds.

The current estimate of the average value of $\zeta$ ($3.5^{+5.3}_{-3.0} \times 10^{-16}$ $s^{-1}$) in the Galaxy is provided by McCall et al. (2003), Indriolo et al. (2007), and Indriolo & McCall (2012) based on $H_3^+$ observations. A similar value of $(5.3 \pm 1.1) \times 10^{-16}$ $s^{-1}$ has been reported by Neufeld & Wolfire (2017). Earlier to the $H_3^+$ revolution, the value of $\zeta$ had been derived using other molecules, such as HD and OH (O'Donnell & Watson 1974; Black & Dalgarno 1977; Hartquist et al. 1978; Federman et al. 1996). However, $H_3^+$ gives a higher value than other methods, and the value of $\zeta$ varies by nearly an order of magnitude across the Galaxy Indriolo & McCall (2012). Le Petit et al. (2016) and Oka et al. (2019) reported even higher values in the central molecular zone of the Galaxy. In addition, Shaw et al. (2016) and Rawlins et al. (2018) reported a higher value of $\zeta$ in high-redshift $H_2$ bearing damped Ly$\alpha$ absorbers.

The $H_3^+$ method relies on measurements of the column density of that molecular ion and needs the electron density in the $H_3^+$ region to derive $\zeta$. It is not possible to measure the electron density directly, so indirect assumptions, described in the next section, have been made. Dalgarno (2006) and Neufeld & Wolfire (2017) examined the chemical reactions that affect $H_3^+$. Here we examine the effects of polycyclic aromatic hydrocarbons (PAHs) on the electron density and determine its impact on determining the value of $\zeta$.

This paper is organized as follows: in Section 2, we describe the $H_3^+$ chemistry and the role of electron density. Our grid of numerical simulations of nine sightlines and the results are presented in Sections 3 and 4, respectively. A discussions and summary are given in Sections 5 and 6, respectively.

## 2. $H_3^+$ Chemistry and Electron Density

### 2.1. Observations and Analytical Analysis

The molecular ion $H_3^+$ is a very important species that can be used to estimate the CR ionization rate (McCall et al. 1998, 2003). In the diffuse interstellar clouds, $H_3^+$ is mainly formed by the CR ionization of $H_2$,

$$H_2 + CR = H_2^+ + e^- \quad (1)$$

followed by proton abstraction reaction producing

$$H_2^+ + H_2 = H_3^+ + H. \quad (2)$$

Whereas $H_3^+$ is destroyed mainly by dissociative recombination processes,

$$H_3^+ + e^- = H + H + H \text{or } H_2 + H. \quad (3)$$

Process 2 is very slow, so in steady state we can write

$$\zeta(H_2) n(H_2) = k_e n(e^-) n(H_3^+). \quad (4)$$

Here, $\zeta(H_2)$ and $k_e$ represent the CR ionization rate of $H_2$ and the electron-recombination coefficient of $H_3^+$, respectively. The terms $n(X)$ represent the number density ($cm^{-3}$) of species X. For a uniform cloud with length $L$ (cm), the densities can be converted into column densities $N$ ($cm^{-2}$) and Equation (4) takes the form

$$\zeta(H_2) = k_e n(e^-) N(H_3^+)/N(H_2)\ [\ s^{-1}]. \quad (5)$$

Defining the molecular fraction as

$$f = 2N(H_2)/N(H), \quad (6)$$

one gets

$$\zeta(H_2) = 2k_e n(_e) N(H_3^+)/fN(H)[\ s^{-1}]. \quad (7)$$

Indriolo & McCall (2012) observed $H_3^+$ in absorption along 50 diffuse sightlines and derived the column densities needed to evaluate Equation (7). The observed column densities of $H_3^+$ are distributed over a range $5 \times 10^{13}$–$3.7 \times 10^{14}$ $cm^{-2}$. An electron density is required to derive the CR ionization rate.

Indriolo et al. (2007) and Indriolo & McCall (2012) derived $\zeta(H_2)$ by assuming $f = 0.67$. In reality, a large range in $f$ is possible so there is significant uncertainty in estimating the values of $f$ and $n(H)$. van Dishoeck & Black (1986) showed that in diffuse clouds, nearly all carbon is singly ionized. Indriolo et al. (2007) further assumed that in diffuse clouds nearly all electrons are produced via the ionization of C to $C^+$ and C/H should approximate the electron fraction, $e^-/H$, that is, $n_e = n(C^+)$. They assumed a single average value, $n_e/n(H) = 1.4 \times 10^{-4}$, for all of their calculations and derived a high value for $\zeta(H_2)$ compared to earlier estimates.

### 2.2. Numerical Methods

Diffuse clouds show structures like photodissociation regions (PDRs) (Tielens & Hollenbach 1985). Hence, we first investigate the above-mentioned assumptions regarding electron density for a standard PDR model. Then we perform detailed numerical simulations of nine sightlines, which are discussed later, to estimate an average CR ionization rate.

All the models presented here are calculated using spectroscopic simulation code, CLOUDY (Shaw et al. 2005, 2020; Ferland et al. 2013, 2017). For this work, we have updated the following rate coefficients for the reactions involving $H_3^+$,

$$H_3^+ + CO = H_2 + HCO^+ \quad (8)$$

$$H_3^+ + CO = H_2 + HOC^+ \quad (9)$$

$$H_3^+ + O = H_2 + OH^+ \quad (10)$$

$$H_3^+ + N_2 = H_2 + HN_2^+. \quad (11)$$

These rates are from Klippenstein et al. (2010) and Rakshit (1982), respectively. The reaction rates for Equations (2) and (3) are taken from Theard & Huntress (1974) and McCall et al. (2004), respectively. McCall et al. (2004) provides the total dissociative recombination rate for the products (Equation (3)). UMIST RATE12 (http://udfa.ajmarkwick.net) provides a branching ratio of 0.53:1. The branching ratios of any product reaction rate is important. Though a branching ratio of 0.53:1 works for the models discussed here, it introduces instability in chemical networks for primordial intergalatic medium (IGM) models. In CLOUDY, we use a branching ratio of 0.25:1. For other atomic, ionic, and molecular processes, CLOUDY utilizes five distinct databases (Shaw et al. 2005; Gay et al. 2012; Porter et al. 2012; Lykins et al. 2015).

We use the size-resolved PAHs, distributed into 10 size bins, and the size distribution of the PAHs is taken from Abel et al. (2008) with minimum and maximum radii of 0.00043 μm (30 C atoms) and 0.0011 μm (500 C atoms), respectively. None-quilibrium heating is important for these small grains, and we include this effect in our calculations. In addition, we also consider the photoelectric effect as well as the charge exchange of PAHs with atoms/ions and electrons to determine the charge of the PAHs. Inner-shell photoionization and the Auger effect of grains and PAHs are also treated following Weingartner et al. (2006). We include the opacity of both neutral and charged PAHs in our calculation with opacities according to Li & Draine (2001), who adopted a thermal approximation. Grains have a net charge, and so they affect the density of free electrons. Our treatment of this physics is described in Abel et al. (2008). In all the models discussed here (if not specified), the temperature is determined from heating and cooling balance involving various terms (Ferland et al. 2017).

### 2.3. Ionization Structure, Electron Density, and Carbon-to-Hydrogen Ratio

We test the assumptions about the electron density by running the standard Leiden PDR models (F1, F2, F3, F4) (Röllig et al. 2007) and finding the predicted $H_3^+$. We find column densities for the F1, F2, F3, and F4 models to be $9.8 \times 10^{14}$, $3.29 \times 10^{14}$, $1.4 \times 10^{13}$, and $1.09 \times 10^{13}$ $cm^{-2}$, respectively. All these models extend up to $A_v = 10$. However, the samples of diffuse cloud considered by Indriolo & McCall (2012) extend less than $A_v = 10$. Hence, as a next step, we run the F1 and F2 models stopping at $N(H_3^+) = 10^{13.8}$ $cm^{-2}$ and check the corresponding $A_v$. We find $A_v = 3.16$ and 6.9 for the F1 and F2 models, respectively. Hence, we consider F1 as a standard model for further investigation as many of the clouds of the Indriolo & McCall (2012) sample have $A_v$ in these ranges, and examine the basis for estimates of the electron fraction to be equal to C/H.

The model F1 is a constant temperature PDR model at 50 K with hydrogen density of $10^3$ $cm^{-3}$ and an impinging radiation field with a strength of 17.0 G0, where G0 is the widely used standard far-UV (FUV) radiation field measured in units of $1.6 \times 10^3$ erg $cm^{-2}s^{-1}$ (Tielens & Hollenbach 1985). The details of this model are discussed in Röllig et al. (2007). The only difference between Röllig et al. (2007) and this work is that here we consider ISM gas phase abundances (Cowie & Songaila 1986; Savage & Sembach 1996; Meyer et al. 1998; Snow et al. 2007), $\zeta(H) = 2 \times 10^{-16}$ $s^{-1}$, and extend the model until $N(H_3^+) = 10^{13.8}$ $cm^{-2}$. Our work does not use the simplified expression for electron density as suggested by Indriolo & McCall (2012). Instead, we use a detailed chemical network with appropriate microphysics (Abel et al. 2008; Ferland et al. 2013).

Figure 1 shows the density of $C^0$, $C^+$, $H^+$, $S^+$, $H_3^+$, and $e^-$ as a function of $A_v$. It is clear from the plot that (i) not all of the carbon is in $C^+$ throughout the entire cloud. Carbon is mostly in the form of $C^+$ at shallower $A_v$ and decreases as $A_v$ increases. (ii) Not all of the electrons are contributed by $C^+$. Ionization of $H^+$, $S^+$, and other metals also contribute to the total electron density. Hence, $e^-/H$ is not equal to C/H. For this model $e^-/H > C/H$.

Figure 2 shows the electron fraction as a function of $n(H_3^+)$ for this model. Initially $n(e^-)/n(H)$ is higher than the assumed

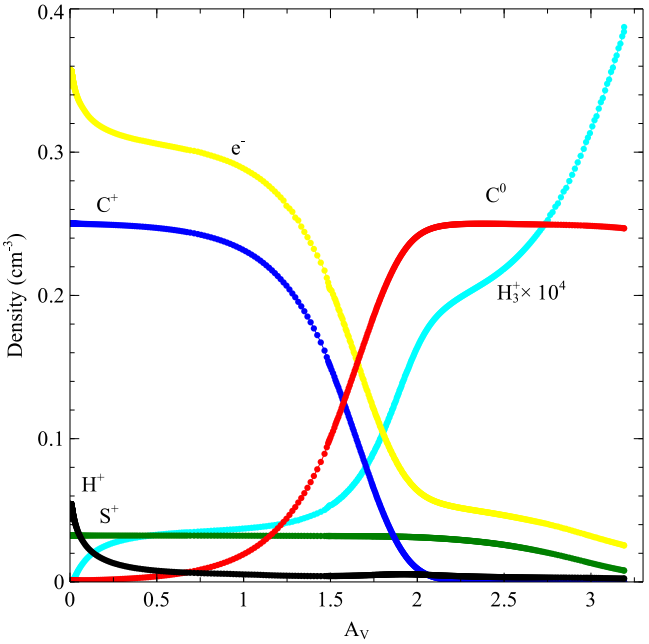


**Figure 1.** Ionization structure for model F1. Density of $C^0$, $C^+$, $H^+$, $S^+$, $H_3^+$, and $e^-$ are plotted as a function of $A_v$.

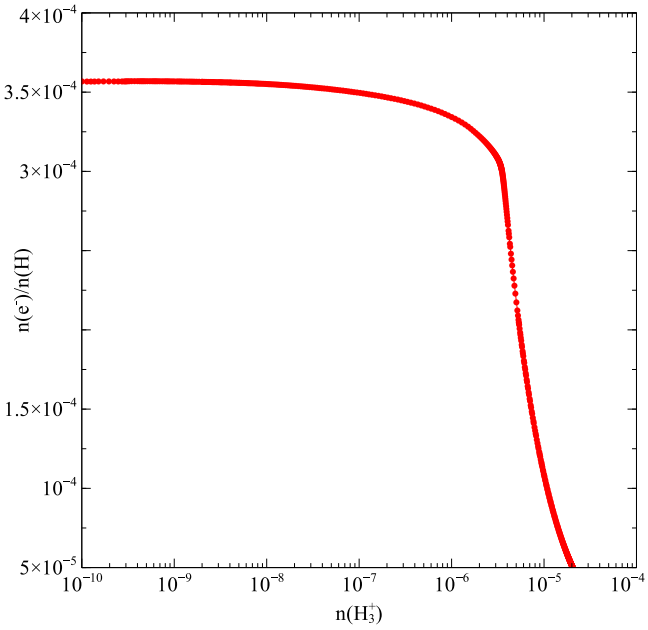


**Figure 2.** $n(e^-)/n(H)$ is plotted as a function of $n(H_3^+)$ for model F1.

C/H abundance ratio of $2.5 \times 10^{-4}$. This is because ions of H, S, and Mg provide electrons besides C. In addition, the electron fraction decreases nearly by a factor 10 at higher $A_v$ where $H_3^+$ forms. This could have a significant impact on the estimate of $\zeta$ (see Equation (7)).

### 2.4. *Effect of the Physical Conditions on Electron Density*

From PDR models it is known that other elements besides C also contribute to the total electron density, depending on the density, impinging radiation fields, and metallicity. Additionally, grains can add or remove electrons from the gas. PAHs also change the electron density due to its high electron affinity (Carelli et al. 2013). Jenkins (2009) has also shown that metals are depleted in different amounts across the Galaxy. In addition, there is an additional positive feedback contribution of electrons from the CR ionization of H, $\zeta$ (H), since the number of secondary electrons that are produced by a primary ionization depends on the electron fraction. It is to be noted here that generally $\zeta(H) = 0.5 \times \zeta(H_2)$. In light of these facts, here we show the effects of various physical conditions on electron density.

As a simple test, we ran the Leiden F1 model varying single parameters, while keeping all the other parameters the same. Unlike the canonical Leiden PDR model, we include PAHs. We varied the radiation field and the CR ionization rate $\zeta$. Figure 3 shows the electron densities as a function of $A_v$ with a radiation field with strength 85 G0 (cyan), $\zeta(H) = 2 \times 10^{-15}$ s$^{-1}$ (green), and PAHs (blue). The default case is shown as the red solid line. For these cases, the shape of the $n(e^-)/n(H)$ versus the $n(H_3^+)$ plot looks similar, but the value of $n(e^-)/n(H)$ is higher. Earlier Shaw et al. (2008) showed that the grain physics play an important role in determining the value of $\zeta$. Small grains neutralize ions and remove free electrons. They also extinguish the FUV radiation field, and hence influence the deduced value of $\zeta$. Indriolo & McCall (2012) assumed a single average value ($1.4 \times 10^{-4}$) for $e^-/H$. For model F1 the value of total hydrogen density is $10^3$ cm$^{-3}$. Hence, their derived electron density would be 0.14 cm$^{-3}$

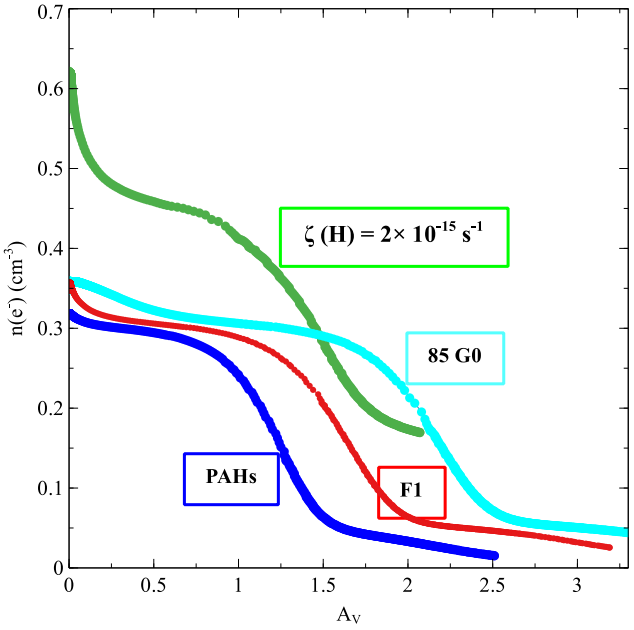


**Figure 3.** The red, cyan, green, and blue solid lines show $n(e^-)$ as a function of $A_v$ for default F1, and with increased radiation field, increased $\zeta$(H), and with PAHs, respectively. All clouds have a thickness that reproduces the same column density in $H_3^+$ ($10^{13.8}$ cm$^{-2}$).

throughout the entire cloud. Considering all these facts, we revisit the value of $\zeta$ by modeling various sightlines with observed column densities of $H_3^+$ and $H_2$, using a detailed numerical simulation.

## 3. Grids of Models

Here we present numerical simulations of nine sightlines from Indriolo & McCall (2012), namely, HD 169454, HD 110432, HD 204827, $\lambda$ Cep, X Per, HD 7388, HD 154368, Cyg OB2 5, and Cyg OB2 12. To minimize uncertainties in

**Table 1**
List of All the Observed Information for the Nine Sightlines Modeled

| Objects | $E(B-V)$ (mag) | $E(B-V)$ References | Density ($cm^{-3}$) | Density References | $N(H_3^+)\pm1\sigma$ ($10^{13}$ $cm^{-2}$) | $N(H_2)\pm1\sigma$ ($10^{20}$ $cm^{-2}$) |
|---|---|---|---|---|---|---|
| HD 169454 | 1.12 | 1 | 300 | 2 | $5.93 \pm 0.34$ | $16.60 \pm 8.37$ |
| HD 110432 | 0.51 | 3 | 140 | 2 | $5.22 \pm 0.17$ | $4.37 \pm 0.29$ |
| HD 204827 | 1.11 | 1 | 450 | 2 | $19.00 \pm 2.54$ | $20.90 \pm 10.20$ |
| $\lambda$ Cep | 0.57 | 2 | 115 | 2 | $7.58 \pm 1.17$ | $6.88 \pm 0.48$ |
| X Per | 0.59 | 2 | 325 | 2 | $7.34 \pm 0.92$ | $8.38 \pm 0.89$ |
| HD 73882 | 0.70 | 4 | 520 | 2 | $9.02 \pm 0.50$ | $12.90 \pm 2.39$ |
| HD 154368 | 0.78 | 4 | 240 | 2 | $9.37 \pm 1.32$ | $14.40 \pm 3.99$ |
| Cyg OB2 5 | 1.99 | 5 | 225 | 2 | $24.00 \pm 3.29$ | $15.20 \pm 7.39$ |
| Cyg OB2 12 | 3.35 | 5 | 300 | 2 | $34.30 \pm 5.89$ | $80.00 \pm 69.10$ |

**References.** (1) Thorburn et al. (2003), (2) Sonnentrucker et al. (2007), (3) Rachford et al. (2002), (4) Rachford et al. (2009), (5) McCall et al. (2002).

modeling, we choose only those sightlines for which the density is derived from observed $C_2$ levels (Sonnentrucker et al. 2007; Rachford et al. 2002). All these sightlines have reported $H_2$ observations and $E(B-V)$. We assume that the classical grains have a Mathis et al. (1977) size distribution. Hence, we consider $R = 3.2$ and calculate $A_v$ as $3.2 \times E(B-V)$. Very little is known about the presence or absence of PAHs along these sightlines.

Table 1 lists all the observed information for the nine sightlines modeled here. For each sightline, we run a grid of models with varying radiation fields and $\zeta$(H) in a step of 0.5 dex. We specify the radiation field in terms of the standard Habing Galactic radiation field (in terms of G0). The shape of the spectral energy distribution is that given by Black et al. (1987) but assuming an extinction of 1–4 Ryd radiation as this is highly absorbed in ISM. Based on the observed $H_3^+$ and $H_2$ column density ($\pm1\sigma$) contours we estimate $\zeta(H_2)$.

In Section 2.4, we mentioned that the electron density depends on the presence of PAHs. PAHs have been detected in various places of our Galaxy with large abundances. However, there are some regions, like the ionized part of the Orion Bar (Sellgren et al. 1990) where PAHs do not exist. In NGC 7023 NW (Montillaud et al. 2013), PAHs with less than 50 carbon atoms are not present. Hence, we perform two sets of calculations for these sightlines. In one set we do not include PAHs, while in the other set we include PAHs. Tielens (2008) determined the abundances of C locked up in PAHs containing 20–100 C atoms as 14 parts per million H atom. As the amount of PAHs is not exactly determined, we consider three different amount of PAHs, depending on Tielens (2008), $PAH_{lo}$, $PAH_{avg}$, and $PAH_{hi}$. The number of PAHs per hydrogen for $PAH_{lo}$, $PAH_{avg}$, and $PAH_{hi}$ are $10^{-6.85}$, $10^{-6.52}$, and $10^{-6.15}$, respectively.

## 4. Results

In this section, we present our results for nine sightlines using detailed numerical simulations. We create contour plots showing column densities of $H_3^+$ and $H_2$ as functions of $X_{CR}$ and radiation field intensity (in terms of G0). Here, $\zeta(H) = 2 \times X_{CR} \times 10^{-16}$ $s^{-1}$.

Figures 4, 6, 8, 10, 12, 14, 16, 18, and 20 show contour plots of $H_3^+$ and $H_2$ column densities as a function of $X_{CR}$ and radiation field (in terms of G0) for HD 169454, HD 110432, HD 204827, $\lambda$ Cep, X Per, HD 73882, HD 154368, Cyg OB2 5, and Cyg OB2 12 without any PAHs, respectively. The black and blue solid lines represent contour plots of column densities for $H_3^+$ and $H_2$, respectively. Whereas the gray- and cyan-filled areas represent observed column density values for $H_3^+$ and $H_2$, $\pm1\sigma$.

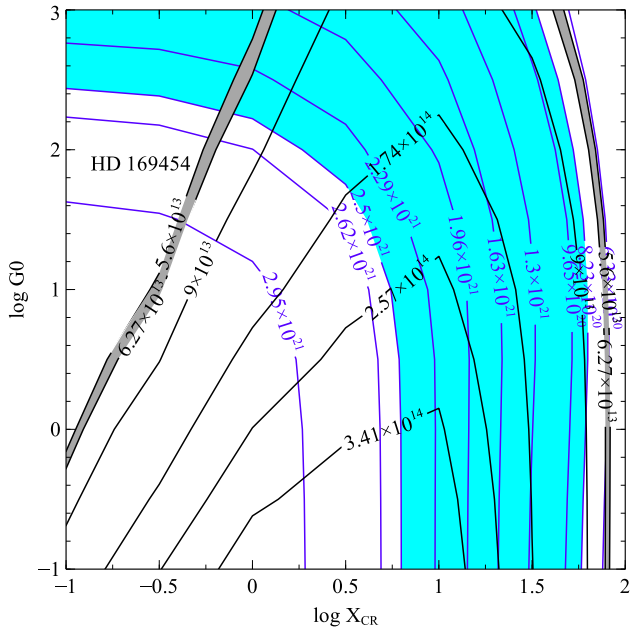


**Figure 4.** Contour plot of $H_3^+$ and $H_2$ as a function of $X_{CR}$ and radiation field (in terms of G0) for HD 169454. The black and blue solid lines represent contour plots of column densities for $H_3^+$ and $H_2$, respectively. The filled areas represent observed column density values $\pm1\sigma$.

In the same manner, Figures 5, 7, 9, 11, 13, 15, 17, 19, and 21 show contour plots of column densities for $H_3^+$ and $H_2$ as a function of $X_{CR}$ and radiation field (in terms of G0) with $PAH_{avg}$ for HD 169454, HD 110432, HD 204827, $\lambda$ Cep, X Per, HD 73882, HD 154368, Cyg OB2 5, and Cyg OB2 12, respectively. Here also the black and blue solid lines represent contour plots of column densities for $H_3^+$ and $H_2$, respectively. Whereas the gray- and cyan-filled areas represent observed column density values for $H_3^+$ and $H_2$, $\pm1\sigma$.

Table 2 lists our findings. The second column of Table 2 shows the predicted value of $\zeta(H_2)$ without considering PAHs in the chemical network. It is clear that without PAHs, except for Cyg OB2 12, most of the sources have $\zeta(H_2) > 10^{-16}$ $s^{-1}$. We estimate an average value of $\zeta(H_2) = (95.69 \pm 46.56) \times 10^{-16}$ $s^{-1}$ for models without PAHs.

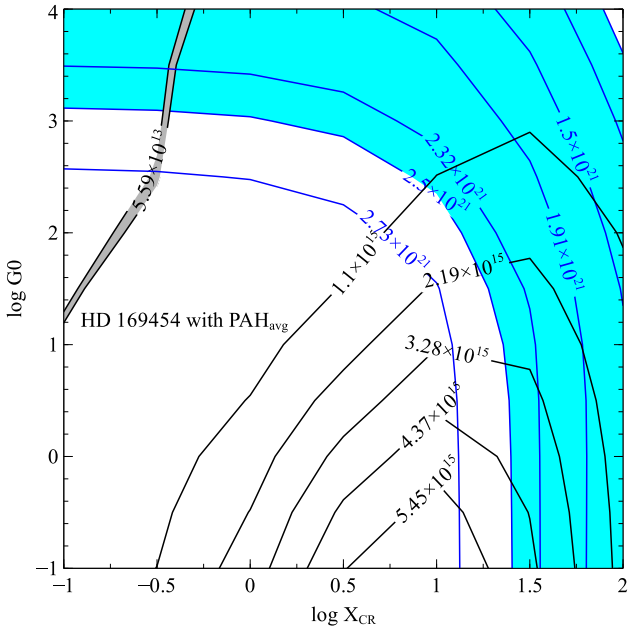


**Figure 5.** Contour plot of $H_3^+$ and $H_2$ as a function of $X_{CR}$ and radiation field (in terms of G0) for HD 169454 with PAHs$_{avg}$. The black and blue solid lines represent contour plots of column densities for $H_3^+$ and $H_2$, respectively. The filled areas represent observed column density values $\pm 1\sigma$.

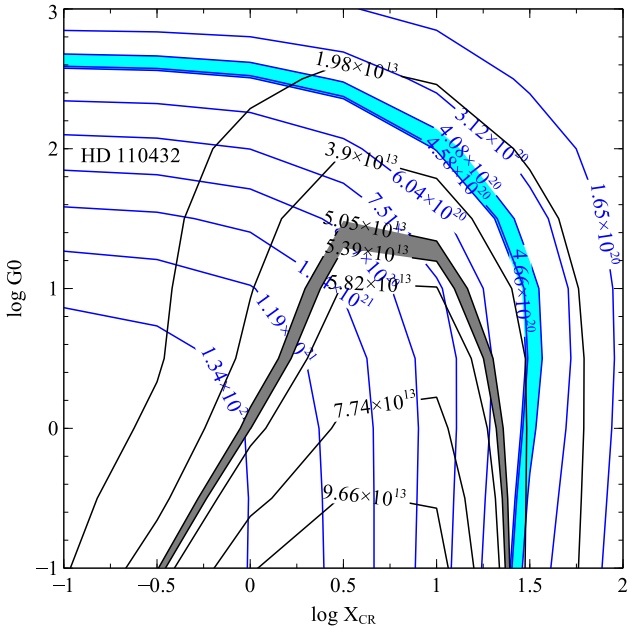


**Figure 6.** Contour plot of $H_3^+$ and $H_2$ as a function of $X_{CR}$ and radiation field (in terms of G0) for HD 110432. The black and blue solid lines represent contour plots of column densities for $H_3^+$ and $H_2$, respectively. The filled areas represent observed column density values $\pm 1\sigma$.

The third column shows the predicted value of $\zeta(H_2)$ with the lower PAH abundance, $PAH_{lo}$ in the chemical network. The presence of PAHs causes the electron density to decrease and the derived value of $\zeta(H_2)$ to decrease. Adding PAHs causes the derived strength of the radiation field to increase. We estimate an average value of $\zeta(H_2) = (75.08 \pm 39.90) \times 10^{-16}$ s$^{-1}$ for models with PAH abundance, $PAH_{lo}$, except Cyg OB2 5 and Cyg OB2 12.

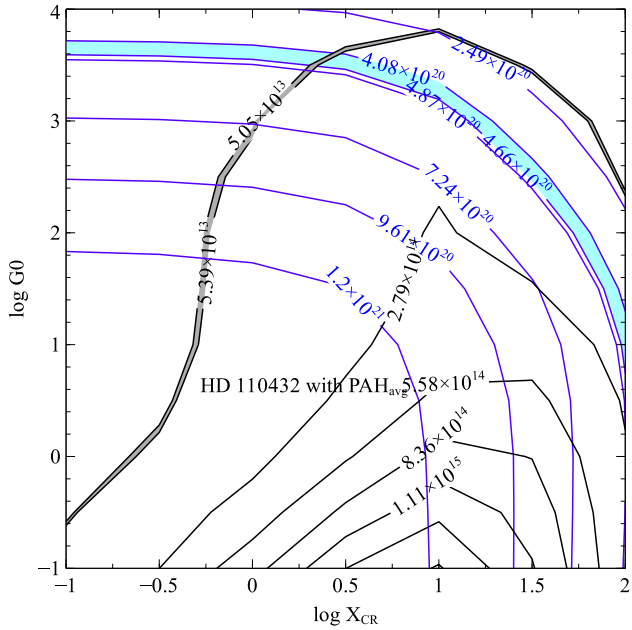


**Figure 7.** Contour plot of $H_3^+$ and $H_2$ as a function of $X_{CR}$ and radiation field (in terms of G0) for HD 110432 with $PAH_{avg}$. The black and blue solid lines represent contour plots of column densities for $H_3^+$ and $H_2$, respectively. The filled areas represent observed column density values $\pm 1\sigma$.

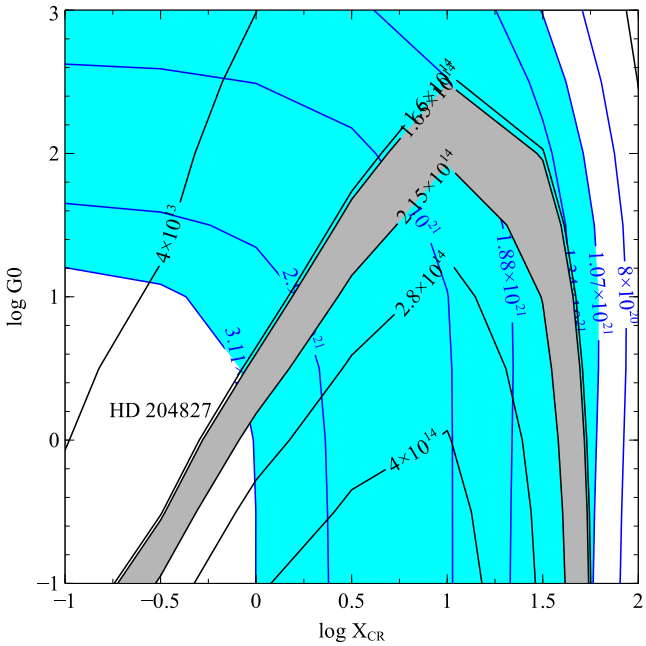


**Figure 8.** Contour plot of $H_3^+$ and $H_2$ as a function of $X_{CR}$ and radiation field (in terms of G0) for HD 204827. The black and blue solid lines represent contour plots of column densities for $H_3^+$ and $H_2$, respectively. The filled areas represent observed column density values $\pm 1\sigma$.

The fourth and fifth columns show the predicted value of $\zeta(H_2)$ with the PAH abundances $PAH_{avg}$ and $PAH_{hi}$, respectively. As expected, the value of $\zeta(H_2)$ decreases further and the derived radiation field also increases. Our contour plots not only provide an estimate of $\zeta(H_2)$, but also an estimate of the prevailing radiation field in terms of G0. The estimated average values of $\zeta(H_2)$ for these two cases are $(7.88 \pm 2.89) \times 10^{-16}$ s$^{-1}$ and

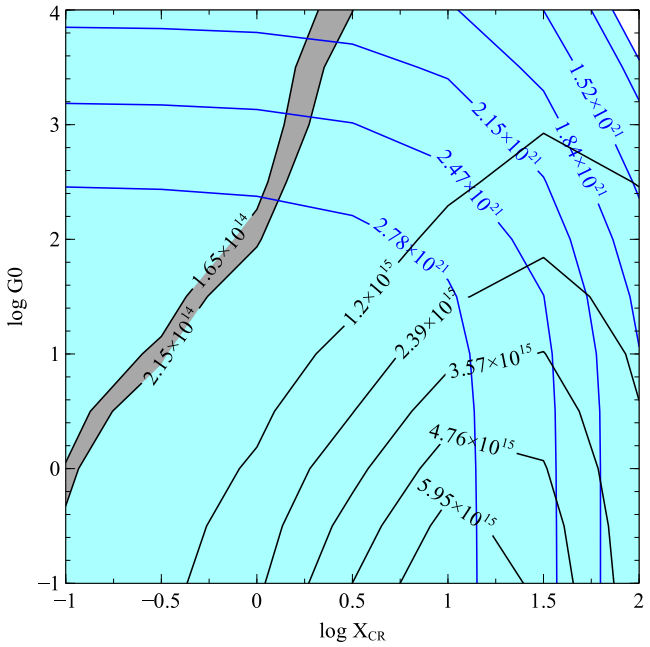


**Figure 9.** Contour plot of $H_3^+$ and $H_2$ as a function of $X_{CR}$ and radiation field (in terms of G0) for HD 204827 with $PAH_{avg}$. The black and blue solid lines represent contour plots of column densities for $H_3^+$ and $H_2$, respectively. The filled areas represent observed column density values $\pm 1\sigma$.

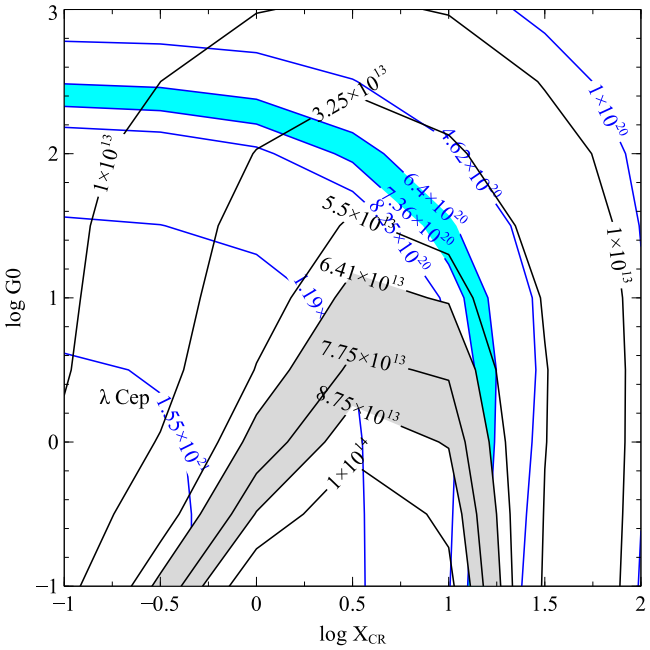


**Figure 10.** Contour plot of $H_3^+$ and $H_2$ as a function of $X_{CR}$ and radiation field (in terms of G0) for $\lambda$ Cep. The black and blue solid lines represent contour plots of column densities for $H_3^+$ and $H_2$, respectively. The filled areas represent observed column density values $\pm 1\sigma$.

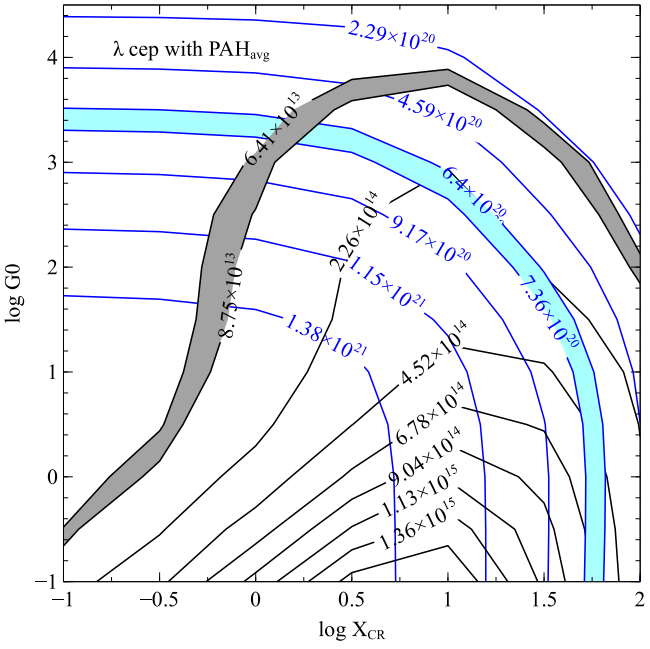


**Figure 11.** Contour plot of $H_3^+$ and $H_2$ as a function of $X_{CR}$ and radiation field (in terms of G0) for $\lambda$ Cep with $PAH_{avg}$. The black and blue solid lines represent contour plots of column densities for $H_3^+$ and $H_2$, respectively. The filled areas represent observed column density values $\pm 1\sigma$.

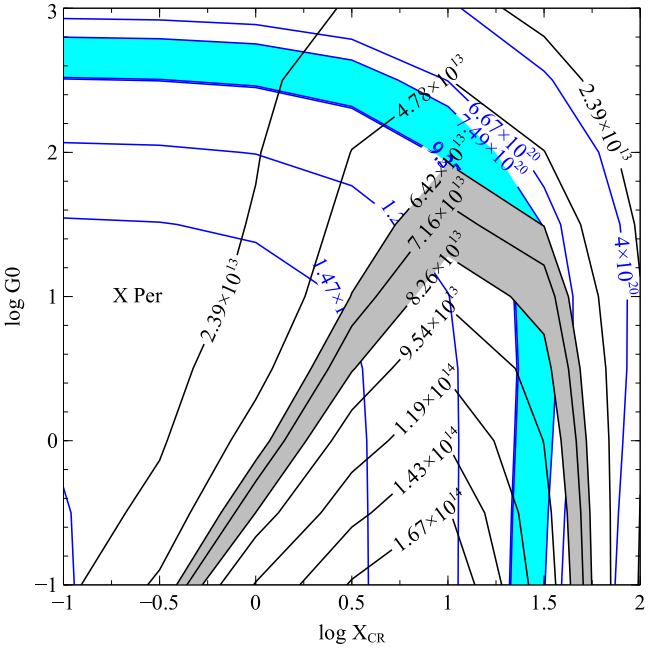


**Figure 12.** Contour plot of $H_3^+$ and $H_2$ as a function of $X_{CR}$ and radiation field (in terms of G0) for X Per. The black and blue solid lines represent contour plots of column densities for $H_3^+$ and $H_2$, respectively. The filled areas represent observed column density values $\pm 1\sigma$.

$(6.50 \pm 3.06) \times 10^{-16}$ $s^{-1}$, except Cyg OB2 5 and Cyg OB2 12. Column six lists the predicted values of $\zeta(H_2)$ by Indriolo & McCall (2012) for comparison. Except for the two Cyg OB2 associations, the values of $\zeta(H_2)$ match that predicted by Indriolo & McCall (2012) within the error bars when $PAH_{avg}$ are considered. We predict ≈1 dex smaller $\zeta(H_2)$ for the Cyg OB2 12 association than predicted by Indriolo & McCall (2012).

## 5. Discussion

Neufeld & Wolfire (2017) also performed detailed numerical simulations of seven sightlines based on observed column densities of $H_3^+$ and $H_2$ and reported an average value of $(5.3 \pm 1.1) \times 10^{-16}$ $s^{-1}$. They included PAHs in their calculations but did not vary their abundance. It is very important to estimate the amount of PAHs, since the value of the observed column

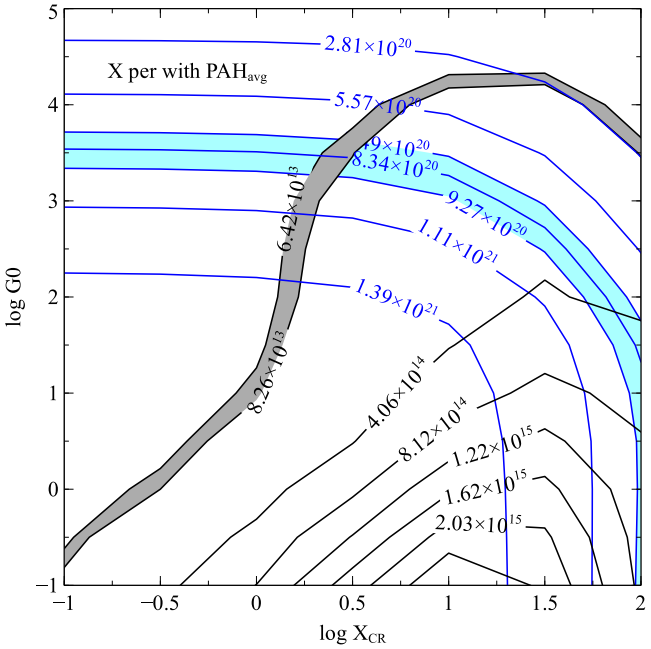


**Figure 13.** Contour plot of $H_3^+$ and $H_2$ as a function of $X_{CR}$ and radiation field (in terms of G0) for X Per with PAH$_{avg}$. The black and blue solid lines represent contour plots of column densities for $H_3^+$ and $H_2$, respectively. The filled areas represent observed column density values $\pm 1\sigma$.

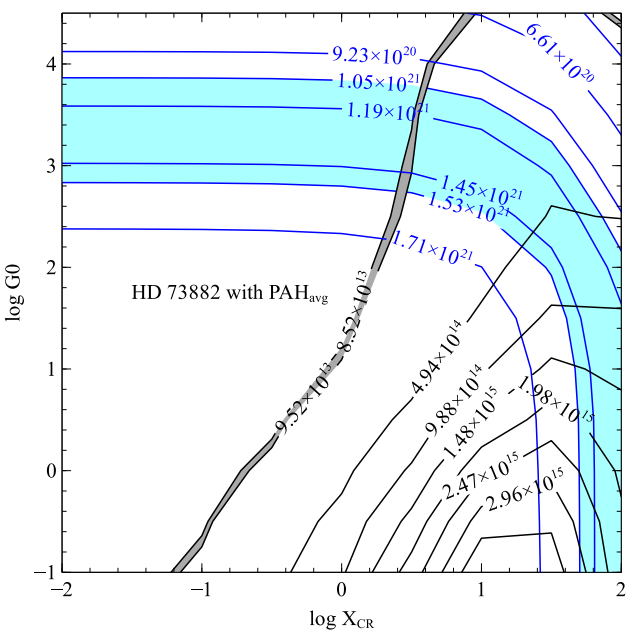


**Figure 15.** Contour plot of $H_3^+$ and $H_2$ as a function of $X_{CR}$ and radiation field (in terms of G0) for HD 73882 with PAH$_{avg}$. The black and blue solid lines represent contour plots of column densities for $H_3^+$ and $H_2$, respectively. The filled areas represent observed column density values $\pm 1\sigma$.

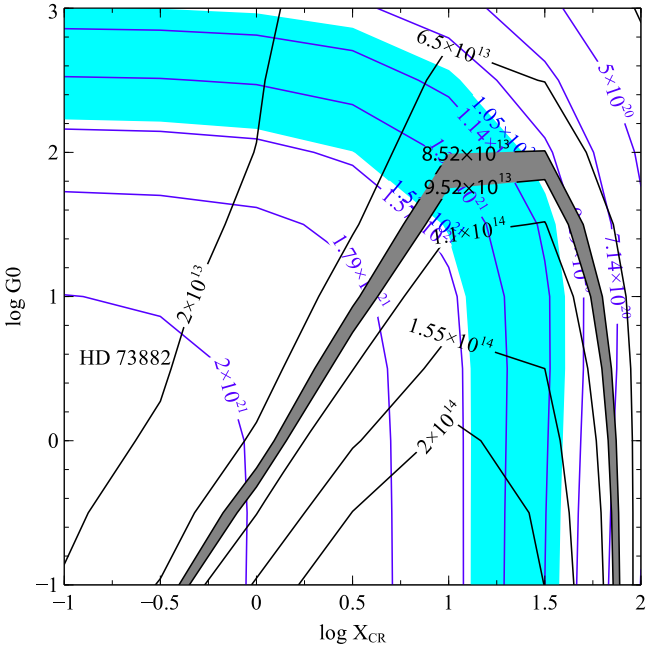


**Figure 14.** Contour plot of $H_3^+$ and $H_2$ as a function of $X_{CR}$ and radiation field (in terms of G0) for HD 73882. The black and blue solid lines represent contour plots of column densities for $H_3^+$ and $H_2$, respectively. The filled areas represent observed column density values $\pm 1\sigma$.

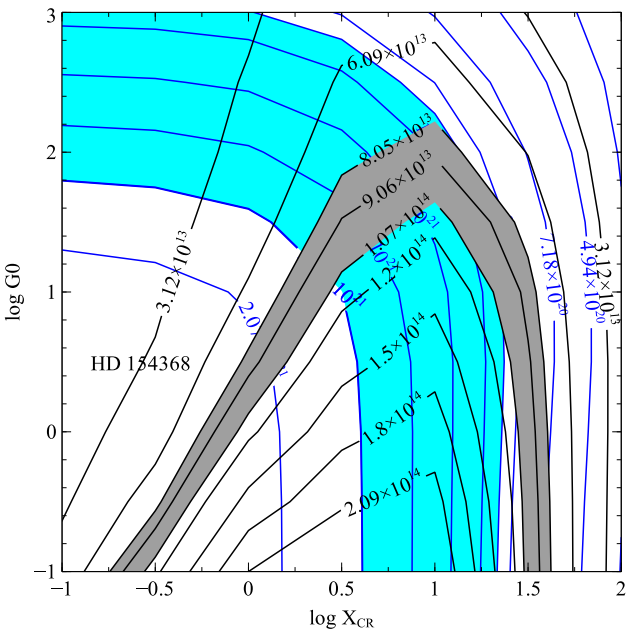


**Figure 16.** Contour plot of $H_3^+$ and $H_2$ as a function of $X_{CR}$ and radiation field (in terms of G0) for HD 154368. The black and blue solid lines represent contour plots of column densities for $H_3^+$ and $H_2$, respectively. The filled areas represent observed column density values $\pm 1\sigma$.

densities of $H_3^+$ and $H_2$ and $\zeta$ depends on it significantly. To illustrate this, we examine the effects of a range of PAH abundances on the molecular abundances in the cloud along the sightline to $\lambda$ Cep. As a baseline model we choose the radiation field ($10^{3.3}$ G0) and $\zeta(H_2)$ ($6.0 \times 10^{-16}$ s$^{-1}$), one of the possible solutions for the PAH$_{avg}$ case described above. Figure 22 shows the results of varying the PAH abundance. The red and blue solid lines represent the predicted column densities for $H_3^+$ and $H_2$, respectively. The red and blue solid-dashed lines represent respective observed column density values $\pm 1\sigma$. It is clear that a factor of 2 change in the PAH abundances will predict column densities beyond the observed range.

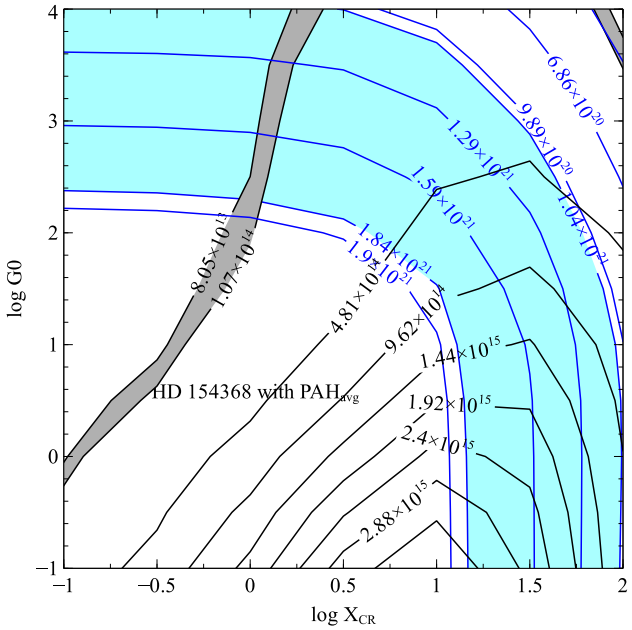


**Figure 17.** Contour plot of $H_3^+$ and $H_2$ as a function of $X_{CR}$ and radiation field (in terms of G0) for HD 154368 with $PAH_{avg}$. The black and blue solid lines represent contour plots of column densities for $H_3^+$ and $H_2$, respectively. The filled areas represent observed column density values $\pm 1\sigma$.

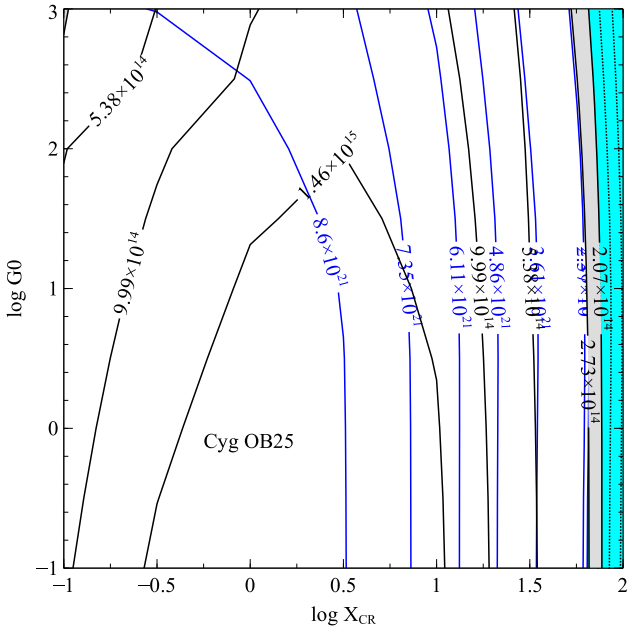


**Figure 18.** Contour plot of $H_3^+$ and $H_2$ as a function of $X_{CR}$ and radiation field (in terms of G0) for Cyg OB2 5. The black and blue solid lines represent contour plots of column densities for $H_3^+$ and $H_2$, respectively. The filled areas represent observed column density values $\pm 1\sigma$.

We note that HD 169454, HD 204827, and the Cyg OB2 12 associations, which have higher $E(B-V)$ than the rest of the sample, predict a smaller value of $\zeta(H_2)$ than the rest with high PAH abundances, $PAH_{hi}$. A similar dependence on $A_V$ was also reported by Neufeld & Wolfire (2017). Though we can compare the predicted values of $\zeta(H_2)$, observed values of the corresponding radiation field are not available. Our typical derived values of G0 are significantly higher than the ISM

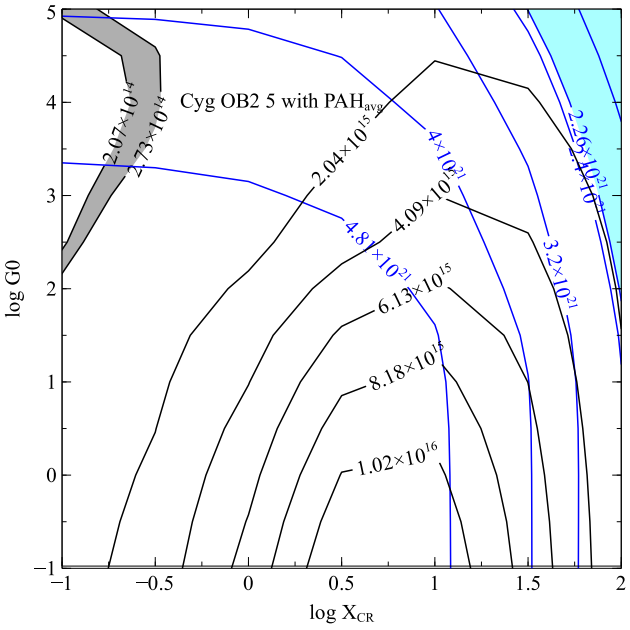


**Figure 19.** Contour plot of $H_3^+$ and $H_2$ as a function of $X_{CR}$ and radiation field (in terms of G0) for Cyg OB2 5 with $PAH_{avg}$. The black and blue solid lines represent contour plots of column densities for $H_3^+$ and $H_2$, respectively. The filled areas represent observed column density values $\pm 1\sigma$. In this case, they do not intersect in the considered parameter space.

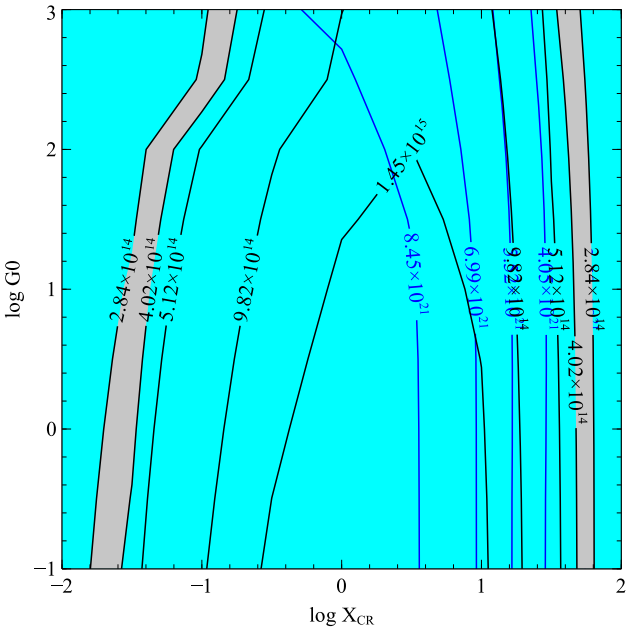


**Figure 20.** Contour plot of $H_3^+$ and $H_2$ as a function of $X_{CR}$ and radiation field (in terms of G0) for Cyg OB2 12. The black and blue solid lines represent contour plots of column densities for $H_3^+$ and $H_2$, respectively. The filled areas represent observed column density values $\pm 1\sigma$.

background, typically G0 10–500, consistent with the clouds being near bright stars.

## 6. Summary

We have used the spectral synthesis code CLOUDY (Ferland et al. 2017) to create detailed simulations of the nine

**Table 2**
CR Ionization Rate

| Objects | $\zeta(H_2)$ This Work no PAHs ($10^{-16}$ s$^{-1}$) | $\zeta(H_2)$ This Work $PAH_{lo}$ ($10^{-16}$ s$^{-1}$) | $\zeta(H_2)$ This Work $PAH_{avg}$ ($10^{-16}$ s$^{-1}$) | $\zeta(H_2)$ This Work $PAH_{hi}$ ($10^{-16}$ s$^{-1}$) | $\zeta(H_2)$ $\pm1\sigma$ Indriolo & McCall (2012) ($10^{-16}$ s$^{-1}$) |
|---|---|---|---|---|---|
| HD 169454 | 2.64 to 5.15 | 2.41 to 4.47 | 1.33 to 2.00 | 0.65 to 0.87 | $2.45 \pm 1.83$ |
| HD 110432 | ≈100.48 | 120.80 to 126.49 | 7.98 to 11.80 | 10.04 to 14.86 | $3.86 \pm 2.10$ |
| HD 204827 | 3.73 to 224.93 | 2.85 to 276.73 | 0.40 to 12.65 | 0.15 to 4.92 | $9.32 \pm 6.92$ |
| $\lambda$ Cep | 50.35 to 63.40 | 59.16 to 76.22 | 4.84 to 8.36 | 4.81 to 8.55 | $2.84 \pm 1.61$ |
| X Per | 30.08 to 123.61 | 29.65 to 152.08 | 7.57 to 14.86 | 6.49 to 13.55 | $5.85 \pm 3.54$ |
| HD 73882 | 28.06 to 111.44 | 24.10 to 89.55 | 9.59 to 15.92 | 0.17 to 13.93 | $9.71 \pm 5.57$ |
| HD 154368 | 7.80 to 89.55 | 6.79 to 79.81 | 3.41 to 9.59 | 1.75 to 10.28 | $4.19 \pm 2.62$ |
| Cyg OB2 5 | 219.00 to 303.43 | 39.08 to 209.92 | … | … | $8.13 \pm 6.03$ |
| Cyg OB2 12 | 0.06 to 258.26 | 0.04 to 317.73 | 0.04 to 0.25 | 0.04 to 0.22 | $2.93 \pm 3.04$ |

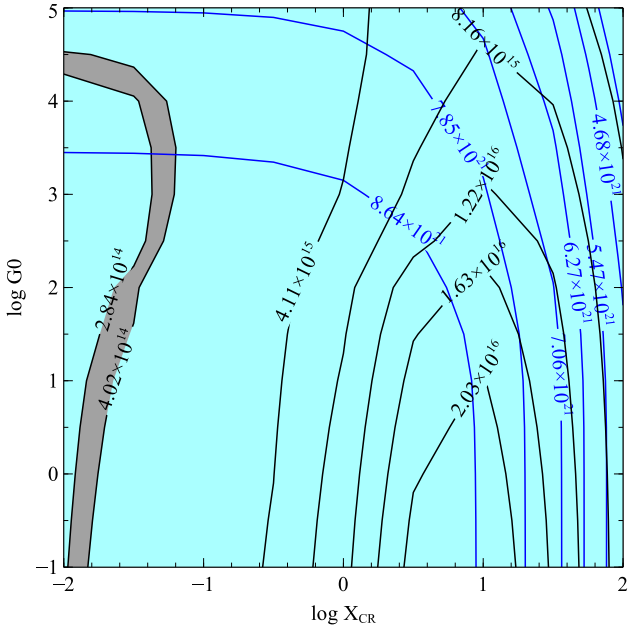


**Figure 21.** Contour plot of $H_3^+$ and $H_2$ as a function of $X_{CR}$ and radiation field (in terms of G0) for Cyg OB2 12 with $PAH_{avg}$. The black and blue solid lines represent contour plots of column densities for $H_3^+$ and $H_2$, respectively. The filled areas represent observed column density values $\pm1\sigma$.

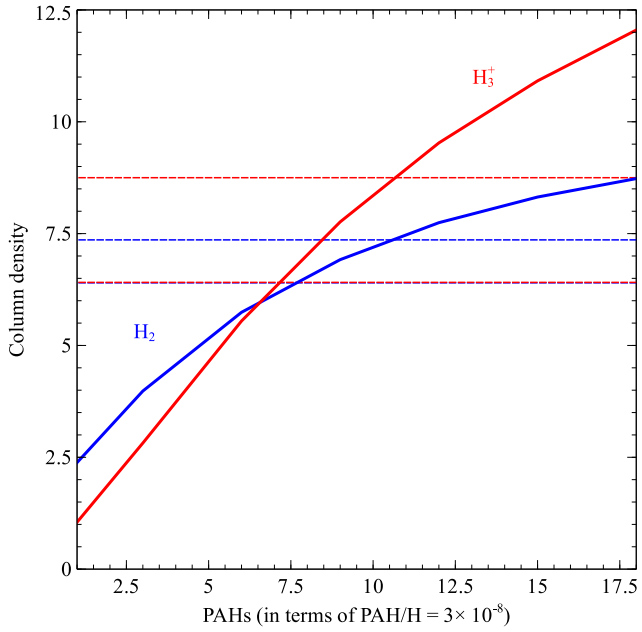


**Figure 22.** Effect of PAHs on the column densities of $H_3^+$ and $H_2$ for the sightline toward $\lambda$ Cep. The red and blue solid lines represent the predicted column densities for $H_3^+$ and $H_2$, respectively. The red and blue-dashed lines represent the respective observed column density values $\pm1\sigma$. Here $H_3^+$ and $H_2$ column densities are scaled by $10^{13}$ and $10^{20}$, respectively.

sightlines toward HD 169454, HD 110432, HD 204827, $\lambda$ Cep, X Per, HD 73882, HD 154368, Cyg OB2 5, and Cyg OB2 12, and determine the value of $\zeta(H_2)$ based on the observed $H_3^+$ and $H_2$ column densities $\pm1\sigma$. Our goal is to determine the CR ionization rate. We also check how sensitive the derived value is to physical assumptions, since, as pointed out by Dalgarno (2006), there are many details in the chemistry that affect the derived quantities.

The electron density plays a pivotal role in determining $\zeta(H_2)$. The physical structure of the clouds along these sightlines is similar to a PDR. Hence, we first studied the electron density and its dependence on various parameters for a standard PDR model, model F1 of the 2006 Leiden PDR workshop (Röllig et al. 2007). Then we performed detailed grid calculations for these nine sightlines. The cloud densities are derived from observed $C_2$ levels (Sonnentrucker et al. 2007; Rachford et al. 2002), and the cloud thicknesses are set from the observed $E(B-V)$.

Very small grains or large molecules can become charged and affect the free electron density and derived CR ionization rate. Although PAHs are very important, their presence or absence is difficult to determine from absorption-line data, and we know that there are some regions, the ionized part of the Orion Bar and NGC 7023 NW, where PAHs and PAHs with less than 50 C atoms are not present, respectively. Hence, to study the effect of PAHs on the derived CR ionization rate, we consider four separate cases, without PAHs and with three values of the PAH abundances. We then solve for the CR ionization rate and radiation field intensity. The values of $\zeta$ for these sightlines differ significantly with and without PAHs.

Our main conclusions are listed below:

1. The common assumption that all carbon is in $C^+$ in regions where $H_3^+$ forms is not true in detail. Carbon is mostly $C^+$ at shallower $A_V$ but becomes neutral or molecules as $A_V$ increases (see Figure 1).

2. The common assumption that all electrons are contributed by $C^+$ where $H_3^+$ forms is not true in detail. The total electron density is affected by the ionization of $H^+$, $S^+$, and other metals, and by the effects of PAHs. Hence, $e^-/H$ is not equal to C/H. For instance, we find that, for the Leiden F1 model, $n(e^-)/n(H) > n(C)/n(H)$ (see Figure 1).
3. We show that the electron density depends on the radiation field, the presence of big molecules (PAHs) or very small grains, and $\zeta$. This affects the $H_3^+$ abundance and derived $\zeta(H_2)$.
4. We predict an average CR ionization rate $\zeta(H_2)$ equal to $(75.08 \pm 39.90) \times 10^{-16}$ s$^{-1}$, $(7.88 \pm 2.89) \times 10^{-16}$ s$^{-1}$, and $(6.50 \pm 3.06) \times 10^{-16}$ s$^{-1}$ for our $PAH_{lo}$, $PAH_{avg}$, and $PAH_{hi}$ cases, respectively, except the two sightlines toward the Cyg OB2 associations.
5. We estimate an average value of $\zeta(H_2) = (95.69 \pm 46.56) \times 10^{-16}$ s$^{-1}$ for models without PAHs.
6. Our derived value of $\zeta$ is nearly 1 dex smaller for the sightline toward Cyg OB2 12 than the value predicted by Indriolo & McCall (2012) with $PAH_{avg}$ and $PAH_{hi}$. A much higher rate, approaching the mean of the previous sightlines, is derived when PAHs are not included. This sightline has a highly uncertain $H_2$ column density. The value of $\zeta(H_2)$ has an uncertainty of more than a dex due to this uncertainty.

G.S. acknowledges the WOS-A grant from the Department of Science and Technology (SR/WOS-A/PM-9/2017). G.J.F. acknowledges support by the NSF (1816537, 1910687), NASA (ATP 17-ATP17-0141, 19-ATP19-0188), and STScI (HST-AR-15018). We thank the anonymous referee for his/her thoughtful suggestions.

## ORCID iDs

Gargi Shaw https://orcid.org/0000-0003-4615-8009
G. J. Ferland https://orcid.org/0000-0003-4503-6333

## References

Abel, N. P., van Hoof, P. A. M., Shaw, G., Ferland, G. J., & Elwert, T. 2008, ApJ, 686, 1125
Black, J. H., & Dalgarno, A. 1977, ApJS, 34, 405
Black, J. H. 1987, in Interstellar Processes, ed. D. J. Hollenbach, J. Thronson, & A. Harley (Dordrecht: Springer), 731
Carelli, F., Grassi, T., & Gianturco, F. A. 2013, A&A, 549, A103
Cowie, L. L., & Songaila, A. 1986, ARA&A, 24, 499
Dalgarno, A. 2006, PNAS, 103, 12269
Federman, S. R., Weber, J., & Lambert, D. L. 1996, ApJ, 463, 181
Ferland, G. J., Chatzikos, M., Guzmán, F., et al. 2017, RMxAA, 53, 385
Ferland, G. J., Porter, R. L., van Hoof, P. A. M., et al. 2013, RMxAA, 49, 137
Gay, C. D., Abel, N. P., Porter, R. L., et al. 2012, ApJ, 746, 78
Hartquist, T. W., Black, J. H., & Dalgarno, A. 1978, MNRAS, 185, 643
Indriolo, N., Geballe, T. R., Oka, T., & McCall, B. J. 2007, ApJ, 671, 1736
Indriolo, N., & McCall, B. J. 2012, ApJ, 745, 91
Jenkins, E. B. 2009, ApJ, 700, 1299
Klippenstein, S. J., Georgievskii, Y., & McCall, B. J. 2010, JPCA, 114, 278
Le Petit, F., Ruaud, M., Bron, E., et al. 2016, A&A, 585, A105
Li, A., & Draine, B. T. 2001, ApJL, 550, L213
Lykins, M. L., Ferland, G. J., Kisielius, R., et al. 2015, ApJ, 807, 118
Mathis, J. S., Rumpl, W., & Nordsieck, K. H. 1977, ApJ, 217, 425
McCall, B. J., Geballe, T. R., Hinkle, K. H., & Oka, T. 1998, Sci, 279, 1910
McCall, B. J., Hinkle, K. H., Geballe, T. R., et al. 2002, ApJ, 567, 391
McCall, B. J., Huneycutt, A. J., Saykally, R. J., et al. 2003, Natur, 422, 500
McCall, B. J., Huneycutt, A. J., Saykally, R. J., et al. 2004, PhRvA, 70, 052716
Meyer, D. M., Jura, M., & Cardelli, J. A. 1998, ApJ, 493, 222
Montillaud, J., Joblin, C., & Toublanc, D. 2013, A&A, 552, A15
Neufeld, D. A., & Wolfire, M. G. 2017, ApJ, 845, 163
O'Donnell, E. J., & Watson, W. D. 1974, ApJ, 191, 89
Oka, T., Geballe, T. R., Goto, M., et al. 2019, ApJ, 883, 54
Porter, R. L., Ferland, G. J., Storey, P. J., & Detisch, M. J. 2012, MNRAS, 425, L28
Rachford, B. L., Snow, T. P., Destree, J. D., et al. 2009, ApJS, 180, 125
Rachford, B. L., Snow, T. P., Tumlinson, J., et al. 2002, ApJ, 577, 221
Rakshit, A. B. 1982, IJMSI, 41, 185
Rawlins, K., Srianand, R., Shaw, G., et al. 2018, MNRAS, 481, 2083
Röllig, M., Abel, N. P., Bell, T., et al. 2007, A&A, 467, 187
Savage, B. D., & Sembach, K. R. 1996, ARA&A, 34, 279
Sellgren, K., Tokunaga, A. T., & Nakada, Y. 1990, ApJ, 349, 120
Shaw, G., Ferland, G. J., Abel, N. P., Stancil, P. C., & van Hoof, P. A. M. 2005, ApJ, 624, 794
Shaw, G., Ferland, G. J., & Ploeckinger, S. 2020, RNAAS, 4, 78
Shaw, G., Ferland, G. J., Srianand, R., et al. 2008, ApJ, 675, 405
Shaw, G., Rawlins, K., & Srianand, R. 2016, MNRAS, 459, 3234
Snow, T. P., Destree, J. D., & Jensen, A. G. 2007, ApJ, 655, 285
Sonnentrucker, P., Welty, D. E., Thorburn, J. A., & York, D. G. 2007, ApJS, 168, 58
Spitzer, L., Jr., & Tomasko, M. G. 1968, ApJ, 152, 971
Theard, L. P., & Huntress, W. T. 1974, JChPh, 60, 2840
Thorburn, J. A., Hobbs, L. M., McCall, B. J., et al. 2003, ApJ, 584, 339
Tielens, A. G. G. M. 2008, ARA&A, 46, 289
Tielens, A. G. G. M., & Hollenbach, D. 1985, ApJ, 291, 722
van Dishoeck, E. F., & Black, J. H. 1986, ApJS, 62, 109
Weingartner, J. C., Draine, B. T., & Barr, D. K. 2006, ApJ, 645, 1188